

Research paper

High-resolution melt pool thermal imaging for metals additive manufacturing using the two-color method with a color camera

Alexander J. Myers^{a,1}, Guadalupe Quirarte^{a,1}, Francis Ogoke^a, Brandon M. Lane^b, Syed Zia Uddin^a, Amir Barati Farimani^a, Jack L. Beuth^a, Jonathan A. Malen^{a,*}

^a Department of Mechanical Engineering, Carnegie Mellon University, 5000 Forbes Avenue, Pittsburgh, 15213, PA, USA

^b Intelligent Systems Division, Engineering Laboratory, National Institute of Standards and Technology, 100 Bureau Drive, Gaithersburg, 20899, MD, USA

ARTICLE INFO

Keywords:

Two-color method
Laser powder bed fusion (LPBF)
Melt pool temperature
Thermal imaging
FLOW-3D®
In-situ process monitoring

ABSTRACT

We introduce an experimental method to image melt pool temperature with a single commercial color camera and compare the results with multi-physics computational fluid dynamic (CFD) models. This approach leverages the principle of two-color (i.e., radiometric) thermal imaging, which is advantageous because it negates the need for a priori knowledge of melt pool emissivity, plume transmissivity, and the camera's view factor. The color camera's ability to accurately measure temperature was validated with a National Institute of Standards and Technology (NIST) blackbody source and tungsten filament lamp between temperatures of 1600 K and 2800 K. To demonstrate the technique, an off-axis high-speed color camera operating at 22 500 frames per second capturing a 2.8 mm × 2.8 mm area on the build plate was used to image both no-powder and powder single beads on a commercial laser powder bed fusion machine. Melt pool temperature fields for 316L stainless steel at varying processing conditions show peaks between 3300 K and 3700 K depending on the laser power and increased variability in the presence of powder. Measurements of nickel superalloy 718 and Ti-6Al-4V show comparable temperatures, with increased plume obstruction, especially in Ti-6Al-4V due to vaporization of aluminum. Multi-physics CFD models are used to simulate metal melt pools but some parameters such as the accommodation and Fresnel coefficients are not well characterized. Fitting a FLOW-3D® CFD model to ex-situ measurements of the melt pool cross-sectional geometry for 316L stainless steel identifies multiple combinations of Fresnel coefficient and accommodation coefficient that lead to geometric agreement. Only two of these combinations show agreement with the thermal images, motivating the need for thermal imaging as a means to advance validation of complex physics models. Our methodology can be applied to any color camera to better monitor and understand melt pools that yield high-quality parts.

1. Introduction

This work focuses on the laser powder bed fusion (LPBF) metal-based additive manufacturing (AM) process, in which powder is spread over a build area and fused to the previous layer with a high-powered laser. Although LPBF is regarded as a mature AM technology, it continues to rely on the empirical selection of process parameters and component design [1]. Despite the rapid advancement of metal AM, several issues identified by early researchers remain, including thermal management problems, porosity, and cracking, which can lead to unsuitable parts [2]. These concerns have propelled significant research in developing in-situ process monitoring and robust thermal modeling.

Melt pool temperature measurements can be used to identify defect signatures such as keyholing, and cooling rates in the solidification

region can be used to predict resulting microstructure. Advances in thermal-fluid models of the melt pool [3] further increase the need for accurate temperature measurements in and around the melt pool for model validation. In-situ melt pool temperature measurement research in LPBF is limited due to the rapid laser speed (400 mm/s to 3000 mm/s) across the powder bed, small size of the melt pool (0.1 mm to 1 mm), and the high temperature gradients (5 K/μm to 20 K/μm) [1].

High-speed visible spectrum cameras, thermal infrared (IR) cameras, and photodetectors have all been used to measure melt pool temperature for thermodynamic insights into the process. Although the use of thermal cameras provides temperature measurements, these approximations require the assumption of a single emissivity, potentially resulting in large temperature errors. Other thermal monitoring efforts

* Corresponding author.

E-mail address: jonmalen@andrew.cmu.edu (J.A. Malen).

¹ Contributed equally to the work.

have captured the entire build with a wide field of view, but also required accurate local material-dependent emissivity calibrations [2]. With typical LPBF scan velocities of around 1 m/s and a laser spot size of 100 μm , most thermal cameras do not provide the sufficient frame rate, exposure time, and resolution required to capture melt pool level temperature transients. Caprio et al. used an illumination source and a high-speed camera to measure melt pool dimensions, which gave melt pool geometric insight but not the temperature fields [4]. Taherkhani et al. used photodetectors to sense the average intensity of thermal emission from the melt pool, which was then correlated to defects in the parts [5].

Two-color pyrometry for temperature measurements of the LPBF melt pool is another methodology with the key advantage of not requiring the melt pool's emissivity. Ren et al. used a two-color IR pyrometer and finite element analysis model to estimate the spectral variation of emissivity over the two channels [6]. The spot size of the pyrometer was 0.95 mm, which resulted in spatially averaged melt pool temperature measurements. Two-color (i.e., radiometric) thermal imaging converts two-color images to thermal maps (i.e., each pixel is used as a pyrometer) and has been used by combustion communities to capture flame temperatures [7,8], which similar to melt pools, also exhibit dynamic emissivities. Using two high-speed monochrome cameras with different band-pass filters, Hooper successfully applied in-line two-color thermal imaging to measure the melt pool temperature of Ti-6Al-4V in a commercial LPBF machine [1]. One challenge that Hooper encountered with this novel approach was the spatial alignment of the two cameras, which were focused through the mirrors and lenses in the laser's optical path. The larger the deviation of the signal wavelength from the laser wavelength, the more the signal was spatially shifted by the laser optics. In addition, this technique required modification to the machine optics and two high-speed cameras. Vallabh et al. provided an alternative by splitting the signal from the laser optical path into two separate optical arms with different filters. Both arms were imaged using a single monochrome camera [9]. Although the complexity of the system was reduced by using one camera, the challenges associated with the imaging aberrations from the laser optical path remain. In addition, the effective field of view of the thermal imaging system was halved because each optical arm occupied half the sensor. Mitchell et al. used a commercial two-wavelength pyrometer made by Stratonic² to measure melt pool temperature, but the temperature field was averaged over an exposure time of 90 μs [10], over which the laser moved by more than its diameter. In laser-based directed energy deposition processes, which have melt pools that are a magnitude of order larger and slower, color cameras have also been explored to measure melt pool temperatures [11,12].

We herein detail the development and validation of a spatially and temporally resolved temperature measurement tool based on a commercial high-speed color camera. By using a color camera for two-color thermal imaging in LPBF, we mitigate issues of misalignment in the laser's optical path while maintaining high spatial and temporal resolution. This method reduces the challenges associated with aligning multiple cameras and eliminates the need for extensive spatial correction by using a camera sensor with a built-in color pixel filter array. Additionally, the portability of the setup allows the system to be moved between machines and validated with a blackbody cavity radiator. Melt pool thermal maps obtained using this tool on a commercial LPBF machine with 316L stainless steel (SS) show maximum measured temperatures in the center of the melt pool between 3300 K and 3700 K. A comparison of the experimental temperature measurements

is made to a FLOW-3D[®] computational fluid dynamics (CFD) model. Although multiple FLOW-3D[®] input parameter combinations yield reasonable geometric agreement with ex-situ melt pool dimensional measurements, the resulting temperature profiles differ substantially. Experimental temperature measurements can hence be used to narrow model parameters selection and better understand the complex physics in the melt pool.

2. Methods

2.1. Two-color method

Planck's law governs the spectral intensity of electromagnetic radiation emitted from a blackbody at a given temperature. It relates the blackbody spectral radiance, or the flux of power emitted by the body per unit wavelength, per unit area, per unit solid angle, $L_{\lambda,b}$, to temperature by

$$L_{\lambda,b}(T) = \frac{c_{1L}}{\lambda^5 [\exp(\frac{c_2}{\lambda T}) - 1]}, \quad (1)$$

where $c_{1L} = 1.191 \cdot 10^{-4} \text{ W } \mu\text{m}^2/\text{sr}$ and $c_2 = 1.439 \cdot 10^4 \mu\text{m K}$. The total emissive power of a blackbody is found by integrating Eq. (1) over all wavelengths and solid angles and according to the Stefan-Boltzmann law, is equivalent to σT^4 . The wavelength at which a blackbody has its maximum spectral emissive power can be found from Wein's displacement law. For common AM metals with melting temperatures around 1700 K and vaporization temperatures below 4000 K, the maximum spectral emissive power occurs between approximately 1.7 μm for melting and 0.7 μm for vaporization. This temperature range permits the use of conventional silicon-based complementary metal-oxide-semiconductor (CMOS) image sensors, which are sensitive to the visible near infrared (VNIR) portion of the spectrum [1].

Unlike a blackbody, AM metals have temperature and wavelength dependent emissivities, $\epsilon(\lambda, T)$. Emissivity is a measure of a body's ability to emit thermal radiation as compared to a blackbody. Emissivity is dependent on material, wavelength, temperature, and surface finish, among other factors. As a result, the actual spectral radiance of a non-ideal surface is $L_{\lambda}(\lambda, T) = \epsilon(\lambda, T)L_{\lambda,b}(T)$. If the emissivity is unknown, the temperature cannot be uniquely determined by integrating L_{λ} over a single wavelength range as done by a monochromatic detector (e.g., conventional IR imaging).

For a given detector, the spectral irradiance on the sensor pixel i , G_i , is also dependent on optical losses (e.g., lenses), $\tau(\lambda)$, and can thus be expressed as

$$G_i(\lambda, T_i) \propto \tau(\lambda)\epsilon_i(\lambda, T_i)L_{\lambda,b}(T_i), \quad (2)$$

where T_i is the average temperature indicated by the i th pixel. The signal of a pixel can be found by multiplying the spectral irradiance by the detector's relative spectral sensitivity, $w(\lambda)$, and integrating over wavelength. Then, for a sensor with a linear response to irradiance, multiplying by the exposure time, Δt , which is the amount of time for which the detector is exposed to the irradiation. The signal of a pixel is expressed as

$$S_i(T_i, \Delta t) = C \Delta t \int_{\lambda} w(\lambda)G_i(\lambda, T_i)d\lambda, \quad (3)$$

where the integrand is the sensed spectral irradiance and C is the constant of proportionality, which accounts for the view factor, detector gain, detector true quantum efficiency, and other linear factors. Using this equation to calculate T_i requires knowledge of the emissivity as a function of wavelength and temperature and the view factor as a function of position. A color camera consisting of red (R), green (G), and blue (B) filtered pixels will have a unique relative spectral sensitivity for each color, $w_{i,R}(\lambda)$, $w_{i,G}(\lambda)$, and $w_{i,B}(\lambda)$. Fig. 1a shows spectral sensitivity provided by the manufacturer for each of the three color filters on the CMOS sensor of the Photron FASTCAM mini-AX200² color camera used here [13].

² Certain commercial equipment, instruments, or materials are identified in this paper to foster understanding. Such identification does not imply recommendation or endorsement by the National Institute of Standards and Technology, nor does it imply that the materials or equipment identified are necessarily the best available for the purpose.

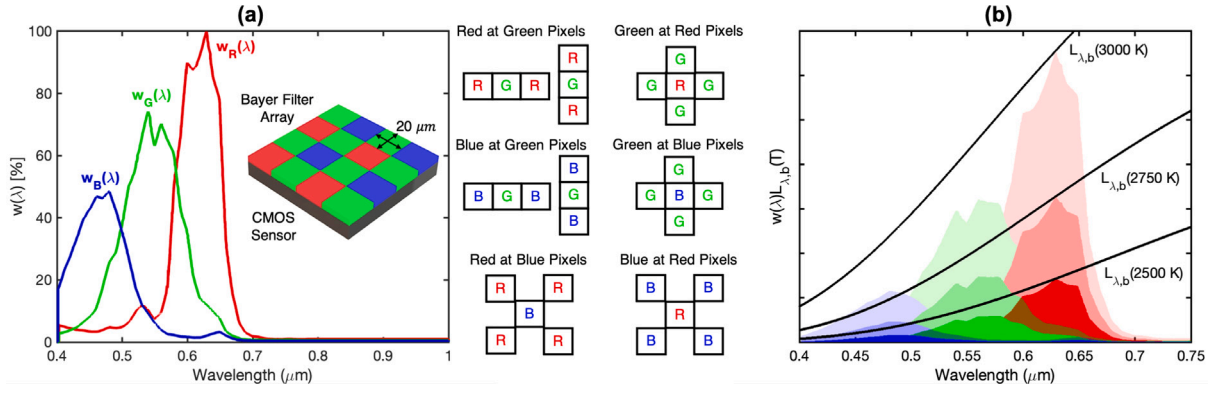


Fig. 1. (a) The relative spectral response of the Bayer filter array for the Photron FASTCAM mini-AX200² color camera [13] and the linear interpolation demosaicing technique used in this work. The proprietary CMOS sensor in this camera uses a Bayer filter array, which consists of two green pixels for each red and blue pixel [14]. In the simple demosaicing algorithm we use, the neighboring pixels are used to find the two missing colors at each pixel. (b) The camera sensor's relative response to blackbody spectral irradiance for three different temperatures.

Taking the ratio of the signals at two colors (e.g., $S_{i,R}/S_{i,G}$) will reduce sensitivity to emissivity, and if emissivity is wavelength independent, it will cancel completely. Qu et al. used eight channels of a hyperspectral camera to approximate the relative spectral emissivity of a Ti-6Al-4V melt pool for temperatures around 1900 K and found that it varies by approximately 15 % between 550 nm and 850 nm [15]. Using reported emissivities close to ambient temperature [16], the variation of spectral emissivity for this system resulted in a predicted temperature error of less than 15 % for all of the materials, temperatures, and primary filtering combination used in this work, as shown in SI.3. With the assumption of constant emissivity across wavelength, the theoretical ratio of the red and green signal, $r_{i,R/G}(T_i)$, as a function of temperature can be expressed as

$$r_{i,R/G}(T_i) = \frac{S_{i,R}(T_i, \Delta t)}{S_{i,G}(T_i, \Delta t)} = C_{R/G} \frac{\int w_{i,R}(\lambda) G_i(\lambda, T_i) d\lambda}{\int w_{i,G}(\lambda) G_i(\lambda, T_i) d\lambda} = C_{R/G} \frac{\int w_{i,R}(\lambda) \tau(\lambda) L_{\lambda,b}(T_i) d\lambda}{\int w_{i,G}(\lambda) \tau(\lambda) L_{\lambda,b}(T_i) d\lambda}, \quad (4)$$

where $C_{R/G}$ accounts for both C_R and C_G . Fig. 1b shows the relative sensed spectral radiance of the three colors for various blackbody temperatures.

2.2. Camera & image processing

To demonstrate our general approach, we use a Photron FASTCAM mini-AX200² color camera [13] set at a frame rate of 22 500 frames/s and field of view (FOV) of 512 pixels by 512 pixels. Because the two-color method of pyrometry relies on the signal output of each pixel, the spectral transmission through all components of the image processing must be understood. In order to sense visible colors, a Bayer filter array, consisting of two green pixel filters for every red and blue pixel filter, covers the sensor. Each pixel senses light from only one color band, resulting in signal outputs unique to each pixel and digitized through a 12-bit (4096 digital levels) analog-to-digital (A/D) conversion in the raw image. In standard color imaging, the signal output from adjacent and different-colored pixels are interpolated using a technique known as demosaicing. Demosaicing algorithms vary in complexity from basic linear interpolation of the nearest neighbors to gradient-based approaches in which the gradients in one color affect the digital level of another color [17]. Fig. 1a shows a Bayer array on a CMOS sensor as well as the basic linear interpolation demosaicing technique used for this work. The raw pixel values obtained prior to Bayer demosaicing from the camera (MRAW) are loaded into Matlab² [18], where additional image processing can be applied. Image processing such as white balance and gamma correction impact the measurements taken with the color camera and are avoided. To verify the linearity of

the camera's digital level with respect to exposure, a technique inspired by Debevec et al. [19] was used in which multiple sets of images of a static scene were taken with varying exposure times. The details of this validation are presented in SI.4. An analysis of the single channels after demosaicing is also shown in SI.5.

2.3. NIST blackbody validation and Tungsten filament verification

Before using the color camera to calculate temperatures of LPPF melt pools, it was calibrated with a blackbody source to determine $C_{R/G}$ from Eq. (4) [20]. Images were taken of the National Institute of Standards and Technology (NIST) AM research lab's calibration blackbody source, an accurate temperature standard to conduct the system calibration [21]. A range of exposure times (δt) from 3.33 μ s to 100 μ s were used for the camera calibration, and 100 images were taken with each exposure time at each calibration temperature. The average signal ratios over all the raw frames for each combination of temperature and exposure time were compared to the theoretical color ratios found from Eq. (4) to find the linear calibration constant, $C_{R/G}$. Combinations of temperature and exposure time with color signal averages below 150 digital levels were discarded due to poor fits with the theoretical calibration curves and high noise levels [22]. Combinations of temperature and exposure time with color signal averages above 4000 digital levels were considered saturated and are also discarded.

The NIST blackbody calibration was conducted for the following three filter combinations, which modify $\tau(\lambda)$: no filters, a tri-band filter (Edmunds Optics² 87–246) with bands centered around 464 nm, 542 nm, and 639 nm, and the tri-band filter with a silicon response flattening filter (Thorlabs² SRF11). The NIST blackbody results compared to the theoretical prediction scaled by the fitted value of $C_{R/G}$ are shown in Fig. 2a. These results validate the use of the Photron FASTCAM mini-AX200² color camera to measure blackbody temperature using the two-color method.

The uncertainty of the high-speed imaging system's calibration temperature measurements, $u_{calibration}(T_{calibration})$, is calculated from the means (μ_R & μ_G) and standard deviations (σ_R & σ_G) of the pixel values from the images taken of the NIST blackbody, and is given by

$$u_{calibration}(T_{calibration}) = \left[\frac{\mu_R}{\mu_G} \sqrt{\left(\frac{\sigma_R}{\mu_R}\right)^2 + \left(\frac{\sigma_G}{\mu_G}\right)^2} \right] \frac{dT}{d(r_{R/G})}. \quad (5)$$

The bracketed term represents the propagation of the channel standard deviations to the uncertainty in the red-to-green ratio, $r_{R/G}$, and $dT/d(r_{R/G})$ is the slope of the fitted calibration curve that maps the uncertainty in $r_{R/G}$ to the uncertainty in temperature. The uncertainty in the temperature measurement increases as the signal decreases because σ_R/μ_R and σ_G/μ_G grow as the signal approaches the noise floor. Using

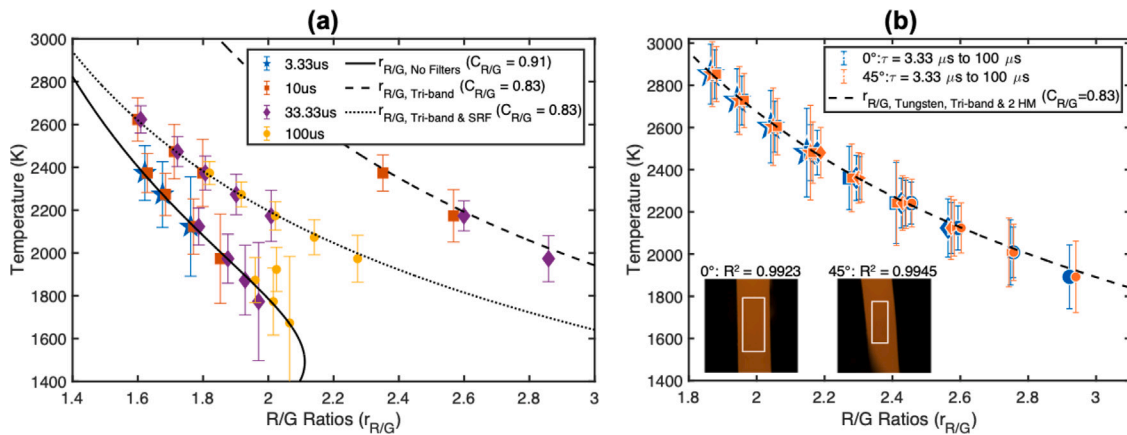


Fig. 2. (a) NIST blackbody temperature calibration curves vs. the red-to-green ratio for varying camera integration times and filter combinations. (b) The tungsten filament verification of the temperature measurement system for the tungsten filament parallel to (blue) and rotated 45° from (orange) the imaging sensor. This verification ensures that the two laser-blocking 750 nm dielectric short pass filters (Edmunds Optics² HM 64–460) do not affect the calibration constant, $C_{R/G}$. The ratio of two colors’ sensed emissive powers yields a temperature-dependent quantity, which is less sensitive to temperature-varying emissivity. The calibration constants, $C_{R/G}$, from Eq. (4) vary with filtering. (For interpretation of the references to color in this figure legend, the reader is referred to the web version of this article.)

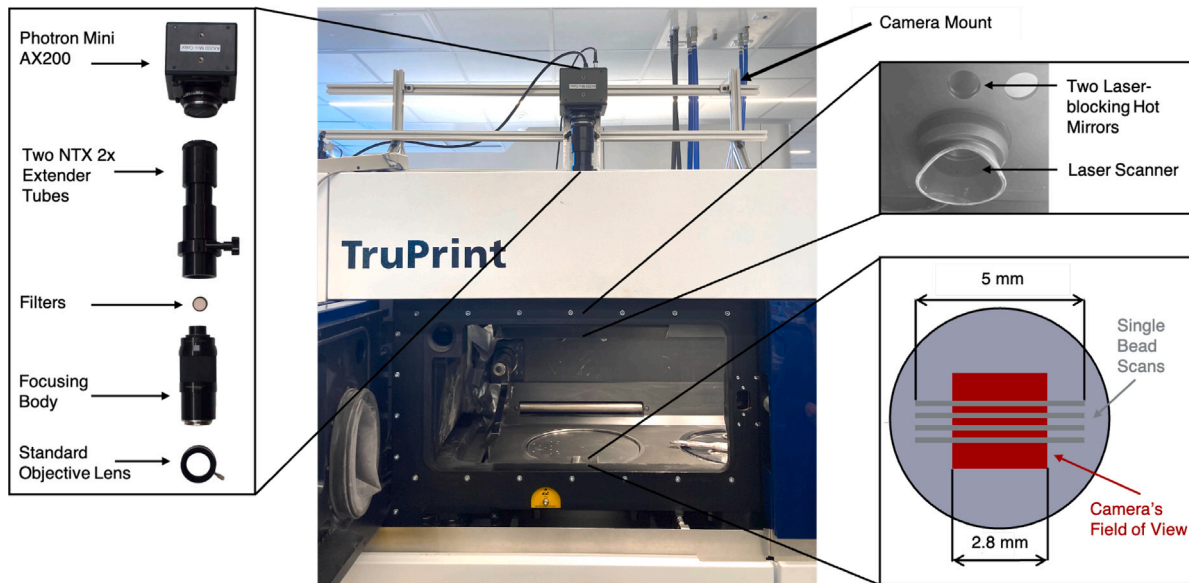


Fig. 3. Photron high-speed camera and optical setup mounted on top of Carnegie Mellon University’s Trumpf TruPrint 3000² LPBF machine. The camera was equipped with an Infinity² K2 DistaMax microscope with two NTX 2x extenders, selected filters (tri-band filter), and the standard objective lens. The camera was aligned off-axis above the front port with two laser-blocking 750 nm dielectric short pass filters, allowing for a top-down view of the build plate. The field of view was 2.8 mm × 2.8 mm, and the single bead scans were at least 5 mm long (up to 15 mm).

the correlation between the signal uncertainty and the signal, which is shown in SI.2, the calibration uncertainty in temperature of a single pixel, $u_{calibration}(T_i)$, can be estimated for any measurement.

After performing the NIST blackbody validation, we performed an additional verification of the color camera temperature measurement system with a calibrated tungsten filament. We used the S8.5–200 tungsten filament lamp from Pyrometer LLC², which has a 3 mm by 12 mm filament viewable through a quartz window and has been calibrated to NIST standards by Pyrometer LLC² for blackbody temperatures ranging from 1073.15 K to 2573.15 K. The camera was equipped with the exact same optical train used in the experimental melt pool measurements (K2 Distamax Lens, tri-band filter and two laser-blocking 750 nm dielectric short pass filters i.e., hot mirrors). At least one hundred images were taken of the tungsten filament and the average signal ratios were compared to the theoretical ratio prediction, $r_{i,R/G}(T_i)$ after accounting for the known spectral and temperature-dependent emissivity of the tungsten filament [16]. To verify that the view factor does not impact the two-color temperature measurement, two orientations of

the filament were tested: surface normal parallel to that of the sensor and 45° from parallel. Fig. 2b shows the verification of both sets of results, which yield identical results. Both orientations have coefficients of determination above 0.99 between the measured and theoretical temperatures, verifying the accuracy of the measurement system for the filter combination used in the melt pool experimental measurements.

2.4. LPBF setup

Metal-based LPBF experiments were conducted on a TRUMPF TruPrint 3000² with and without powder. The camera body was mounted with a Model K2 DistaMax™ Long-Distance magnification lens manufactured by Infinity USA², with two 2x extenders and a standard objective lens (990210), as shown in Fig. 3. The tri-band filter was placed in the magnification lens. The magnification lens and camera were mounted above the machine’s front view port, where the original equipment manufacturer (OEM) process-monitoring camera would typically be installed. The glass on the view port was replaced with two

Table 1
LPBF parameters.

Power	300 W	150 W	450 W
Laser Beam Diameter	100 μm	100 μm	100 μm
Velocity (m/s)	0.4, 0.7, 1.0, 1.6	1.0	1.0
Shielding Gas	1.6 m/s Ar	1.6 m/s Ar	1.6 m/s Ar
Preheat Temperature ($^{\circ}\text{C}$)	26	26	26

Table 2
Camera parameters.

Exposure time	1.05 μs –40 μs
Frame rate	22 500 frames/s
Bit depth	12-bit
Filters	Tri-band & two 750 nm short pass (Hot mirror)

750 nm dielectric short pass filters with a 50 mm diameter (Edmunds Optics² Hot Mirror 64–460) to block reflected laser light, which has a wavelength of approximately 1070 nm. This camera setup offers the ability to accurately view the melt pools directly below the camera while protecting the camera from powder and spatter. The pixel pitch is 20 μm [13], and the optics provide approximately 3.6x magnification, resulting in 5.6 μm per pixel on the build plate. The diffraction limit, based on the longest wavelength red band (approximately 625 nm), numerical aperture (approximately 0.2), and the Rayleigh criterion, is approximately 3.8 μm , indicating that this system's resolution is limited primarily by pixel size, not diffraction. Demosaicing reduces this pixel size limiting resolution [23]. Since we use only neighboring pixels, the effective resolution will be no greater than the 3 by 3 pixel grid (16.8 μm by 16.8 μm).

A velocity series of bare plate, no-powder, 316L SS single bead tracks with a constant power of 300 W were conducted at velocities of 0.4 m/s, 0.7 m/s, 1.0 m/s, and 1.6 m/s and imaged using the two-color thermal imaging system. This no-powder velocity series was repeated on two additional materials: nickel superalloy 718 (In718) and Ti-6Al-4V. Additionally, a power series of no-powder, 316L SS single bead tracks were run with a constant velocity of 1.0 m/s at powers of 150 W, 300 W, and 450 W. In all no-powder experiments, the single bead tracks were programmed to be at least 5 mm long and spaced apart by a minimum of 300 μm to prevent the melt pools from overlapping.

To test the effect of powder on melt pool temperature, another set of single bead tracks with 316L SS powder were run at the same six power and velocity combinations used in the no-powder 316L SS experiments (both the velocity and power series). The 316L SS powder experiments used Hogan's 316L 20 μm to 53 μm diameter powder. The single bead tracks were programmed to be 15 mm long and spaced apart by 360 μm . The powder layer was set to \approx 100 μm , which simulates a 50 μm layer with an assumed powder packing fraction of 50 %. The top of the powder layer was set to the same height as the top of the bare plate in the no-powder experiments.

A range of exposure times were used to capture varying temperatures within the camera's dynamic range, with at least five used for each single bead, totaling over 100 thermally-imaged single bead tracks. For all experiments, the camera's frame rate was set to 22 500 frames/s, providing a FOV of 2.8 mm \times 2.8 mm to capture a large portion of the single bead tracks and test a wide range of exposure times. Videos at frame rates in excess of 60 000 frames/s can be achieved with this setup. The LPBF parameters are summarized in Table 1, and the camera parameters in Table 2. A more detailed drawing of the camera and build plate setup's geometry is shown in SI.7.

3. Results

The no-powder 316L SS melt pool temperature fields for four different scan velocities at a constant power of 300 W and three different exposure times (δt) are shown in Fig. 4. The estimated uncertainty contours show the aggregate of the calibration uncertainty and the uncertainty due to the constant emissivity assumption, as shown in SI.3. As the exposure time is increased, the signal at the center of the melt pool saturates the pixels but the signal in the lower-temperature tail of the melt pool is within the observable dynamic range of the camera, which was previously observed by [1]. A high-temperature band around the front of the melt pool is visible at higher exposure times, which is likely influenced by the plume above the melt pool. Additionally, a comparison of the no-powder 316L SS melt pool temperature fields for three different powers at a constant scan velocity of 1.0 m/s and three exposure times are shown in Fig. 5.

Melt pool temperatures shown in Fig. 4 and Fig. 5 peak between 3300 K and 3700 K, with higher powers resulting in higher peak temperatures. The lowest temperatures observed within the camera's dynamic range are approximately 2050 K, which is around 400 K above the melting point of 316L SS [24]. The elevated lower temperature bound results from the limited dynamic range of the color camera, which requires exposure times of 100 μs to sense blackbody temperatures around the melting point of 316L SS. This lack of sensitivity to low temperatures also limits our ability to calculate the melt pool's length or average surface temperature, preventing a direct comparison to two-color pyrometer measurements that report the average temperature of the entire melt pool. Obstruction of the plume around the head of the melt pool creates uncertainty in the melt pool widths from the melt pool thermal images alone, which was previously observed for monochrome imaging by Stutzman et al. [25]. Color videos and melt pool thermal fields for 316L SS without and with powder are shown in Supplementary Videos 1 and 3 with an exposure time of 1.99 μs and 2 and 4 with an exposure time of 6.67 μs .

A comparison between no-powder 316L SS, In718, and Ti-6Al-4V melt pool thermal fields processed at a velocity of 1.0 m/s and power of 300 W is shown in Fig. 6. The In718 thermal fields show similar melt pool size and temperature to 316L SS under the same process conditions, but the Ti-6Al-4V thermal map has a large saturated region in the center of the melt pool and lower temperatures visible in the tail. Differences between material properties such as emissivity impact the irradiance on the camera sensor for a given temperature. Near room temperature, Ti-6Al-4V has a higher emissivity in the visible spectrum than 316L SS, and a higher emissivity in the red channel than In718 [16]. Although In718 has a more visible plume than 316L SS at a 40 μs exposure time, Ti-6Al-4V has a much larger and brighter plume than both. The larger plume observed in the Ti-6Al-4V thermal maps may be a result of aluminum vaporization, as has been previously reported for electron beam AM [26].

Thermal images are compared in Fig. 7 from five successive frames for both the powder and no powder 316L SS melt pools (velocity of 1.0 m/s and power of 300 W). The addition of powder increases the variability in the melt pool shape and the amount of ejected spatter. The spatter is moving approximately ten times faster than the melt pool [27], which causes significant motion blurring of the temperature field around the edges of the melt pool. For these images, the standard deviation of pixels enclosed by the 2000 K isotherm is 4 % to 8 % of the mean without powder and 13 % to 18 % of the mean with powder, depending on exposure time.

4. Discussion

To understand how well these complex multi-physics CFD models predict the temperature of the melt pool and where they deviate from the experimental two-color temperature measurements, a model was

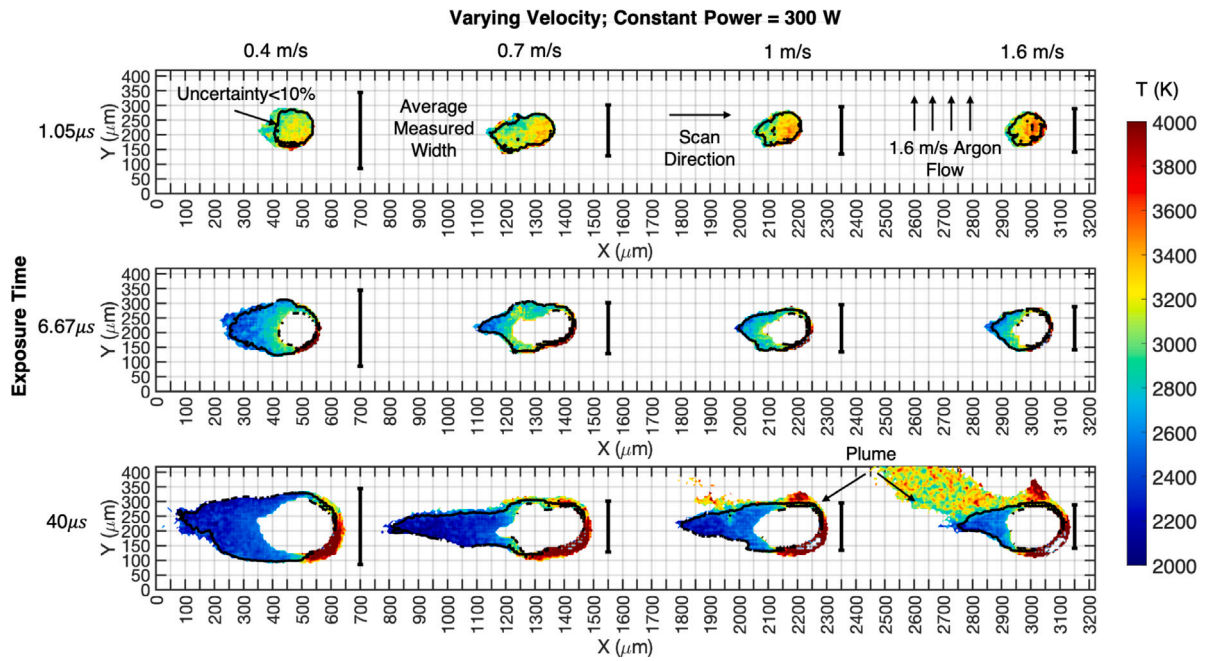


Fig. 4. Melt pool temperature fields for 316L stainless steel calculated from $r_{R/G}$ at varying velocities with a constant power of 300 W imaged with different exposure times without powder. Temperatures are shown where the green pixel values are above 150 digital levels and the red pixel values are below 4000 digital levels. The contour lines enclose the region where the uncertainty in temperature prediction is less than 10%. As the exposure time increases, the center of the melt pool saturates but the tail of the melt pool becomes visible. The plume becomes more visible as the exposure time is increased due to its low signal. Melt pool lengths were not measured because melt pool temperatures below 2000 K were not within the dynamic range of the camera while limiting the exposure time due to motion blurring.

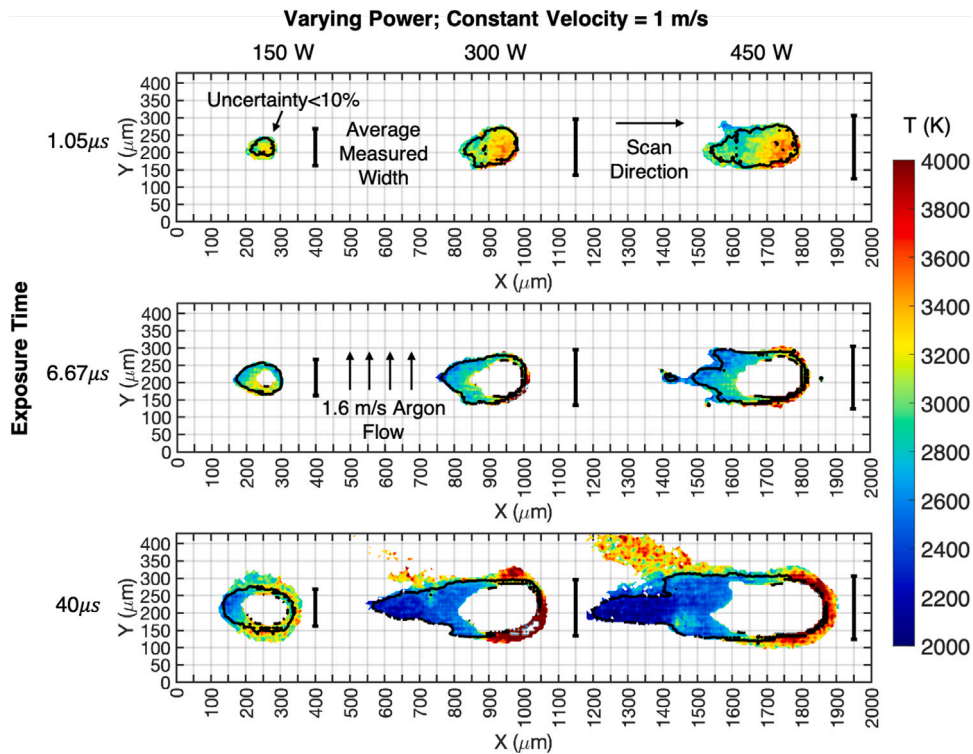


Fig. 5. Melt pool temperature fields for 316L stainless steel calculated from $r_{R/G}$ at varying powers with a constant velocity of 1 m/s imaged with different exposure times without powder. Temperatures are shown where the green pixel values are above 150 digital levels and the red pixel values are below 4000 digital levels. The contour lines enclose the region where the uncertainty in temperature prediction is less than 10%.

developed for the processing conditions in this work. A number of modeling techniques have been developed to predict the temperatures in and around the melt pool. Rosenthal developed a steady-state analytical solution to the temperature field in welding based on heating by a point

source moving over the surface of a semi-infinite solid [28]. Eagar and Tsai derived a semi-analytical transient solution by making the same assumptions as Rosenthal but replacing the point heat source with a normally-distributed heat flux [29]. Although more computationally

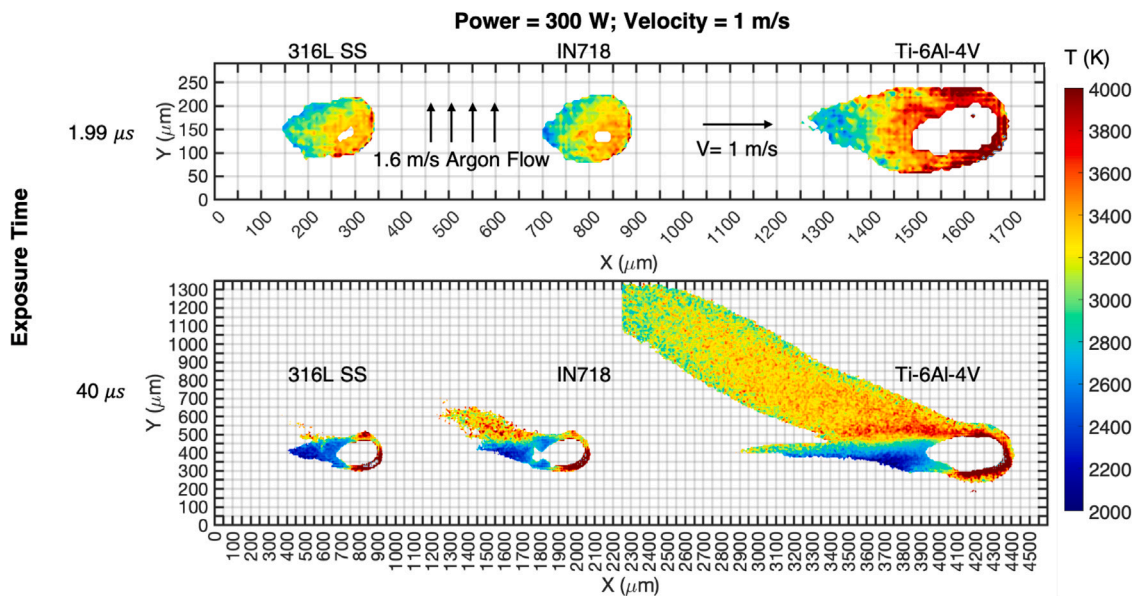


Fig. 6. Melt pool temperature field comparison between 316L stainless steel, IN718, and Ti-6Al-4V at a power of 300 W and scan velocity of 1 m/s with 1.6 m/s argon flow and no powder. Temperatures are shown where the green pixel values are above 150 digital levels and the red pixel values are below 4000 digital levels.

expensive, a transient thermal finite element analysis (FEA) model improves upon both of these analytical solutions with the inclusion of temperature-dependent properties as well as convection and radiation at the melt pool surface [30,31]. These transient thermal solid phase simulations lack both the convection of the molten metal in the melt pool, and the mass and energy transport of the vaporized material into the plume. Cheng et al. include these effects along with the recoil pressure in a CFD modeling package, FLOW-3D® [3]. Gusarov et al., Tran et al., and Cheng et al. use ex-situ cross-sectional single bead cross-sections to validate their melt pool models [3,30,31].

4.1. Comparison to simulation

The FLOW-3D®^{v12.0u2R7} CFD software was used with FLOW WELD v3.01R7 to simulate the melting process [32], in which the coupled partial differential equations describing the mass, momentum, and energy conservation of the system are solved on a Cartesian mesh using the volume of fluid (VOF) model [33,34]. The model simulates a Gaussian heat source on a bare plate and accounts for temperature-dependent density, thermal conductivity, viscosity, and specific heat [24], conduction, convection, radiation [16], fluid effects with constant surface tension, vaporization [35], and Fresnel absorption [36–38]. Some of the theories used in this modeling software are detailed in SI.1. The simulations were conducted without powder and compared to no-powder experiments due to the lower variability in these melt pools, which is more suitable for model parameter fitting. The role of powder on effective absorptivity is a topic of rich debate. In solid-state simulations, multiple reflections between the powder have been shown to increase effective absorptivity [30,31], and experimental results suggest that denuded powder and spatter can cause a reduction in the laser absorption [39].

Two key model parameters, the Fresnel and accommodation coefficients, were fit to all six of the ex-situ cross-sectional areas and the width-to-depth ratio of no-powder 316L SS single bead tracks simultaneously. The objective was for one set of model parameters to fit all six of the power and velocity combinations. The Fresnel coefficient controls the amount of laser radiation absorbed as a function of the incidence angle, and the accommodation coefficient controls the material vaporization, associated heat removal, and resulting recoil pressure (see SI.1). The ex-situ measurements are detailed in SI.6, and

the simulation setup and fitting are detailed in SI.1 along with a parameter summary in Table S1. Once the two coefficients were fit based on the ex-situ geometry, surface temperature profiles near the centerline of melt pool on the top of the plate were compared to composite graphs of experimental two-color temperature measurements taken at various exposure times, as shown in Fig. 8a for a power of 300 W and velocity of 1 m/s. Fig. 8b shows the experimental results and the simulated temperature profiles from models with the lowest average overall cross-sectional and width-to-depth ratio error (< 20 %, see Figure S1). The shaded error regions on the simulation curves are found by averaging over ten time steps (refer to SI.1), and the error bars on the experimental data are an aggregate of the calibration and emissivity uncertainties (refer to SI.3).

Although the simulation with the default steel accommodation coefficient of 0.01 results in a reasonable fit to the single bead geometry (average of area and width-to-depth ratio), the peak melt pool temperatures deviate more from the experimental measurements. Simulations with lower Fresnel coefficients and higher accommodation coefficients predict lower peak temperatures, which agree better with the experimental results. Under the laser, peak temperatures on the surface of the melt pool in the simulation show temperatures significantly above the vaporization temperature of 316L SS (3090 K [35]). These peak temperatures are higher than the temperatures observed by the camera, which observes surface temperatures between 3300 K and 3700 K. The simulation results from the model with an accommodation coefficient of 0.1 and 0.15 and a Fresnel coefficient of 0.2 show more reasonable agreement with the experimental measurements for all power and velocity combinations behind the laser. A cross-section of the simulation thermal results with these parameters is shown in Fig. 8d. The disagreement in front of the melt pool (approximately $x > 50$ mm) is likely due to obstruction by the plume, which challenges overhead thermal imaging approaches. It is also possible that the plume influences temperature measurements directly under the laser, which is where significant vaporization occurs. The experimental and simulation results for the other power and velocity combinations are shown in Fig. 8e–g. All six power and velocity cases tested show similar thermal agreement to the lower Fresnel coefficients and higher accommodation coefficients. By assuming a constant surface tension, the Marangoni effect is neglected in this model. Most of the fluid flow in this melt pool model is driven by the recoil pressure due to vaporization. Khairallah et al. simulate 316L SS LPBF melt pools with temperature-dependent

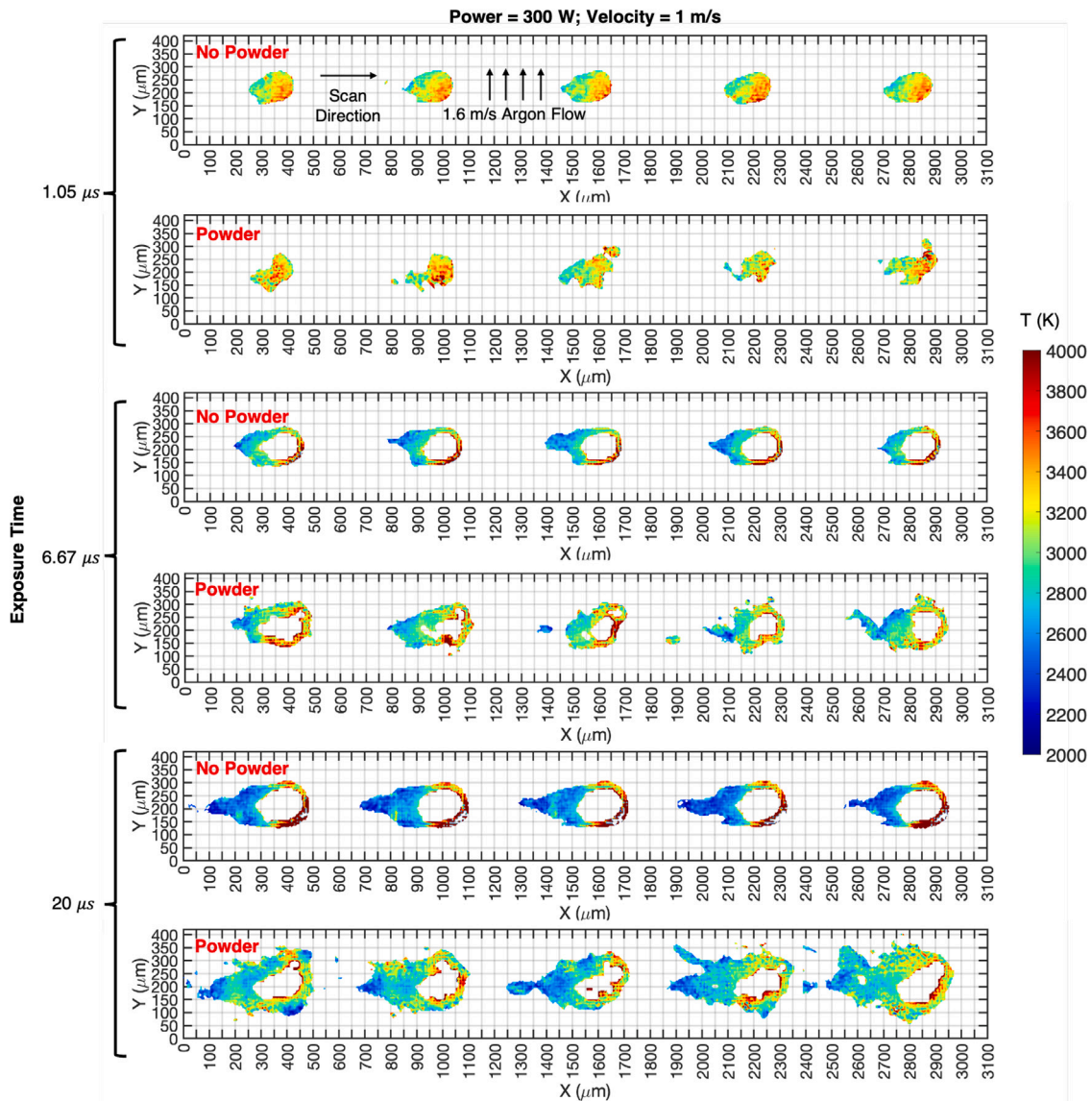


Fig. 7. Comparison of five successive melt pool temperature fields with and without powder on the build plate for 316L stainless steel at a velocity of 1 m/s and power of 300 W imaged with three different exposure times. The addition of powder increases the variability in the melt pool. Temperatures are shown where the green pixel values are above 150 digital levels and the red pixel values are below 4000 digital levels. The melt pool images were taken $44.4 \mu\text{s}$ apart and are spaced out for visualization.

surface tension and predict peak temperatures in excess of 3500 K [40]. Hooper also observes the plume around the outer edge of some melt pool images and measures peak temperatures of approximately 4000 K in Ti-6Al-4V melt pools in hatched and overhanging regions of the part [1].

4.2. Uncertainty and limitations

Uncertainty in temperature and the camera's thermal sensitivity range are key limitations to the current thermal imaging system. The uncertainty in temperature is a function of both the pixel values and the slope of the radiometric response curve, $dT/d(r_{R/G})$ (Fig. 2). At blackbody temperatures around 1600 K, the uncertainty in temperature is dominated by the uncertainty in pixel values due to pixel noise, and at high temperatures, by the flat response curve. The camera's thermal sensitivity is bound at the lower end by the noise floor of the camera, below which thermal and electrical noise dominates the signal [22], and the spectral sensitivity of the color camera sensor. The exposure time can be increased, which increases the signal at lower temperatures, but a higher exposure time also results in more motion

blurring in the image. Fig. 9a shows contours of motion blurring equal to 10 % of the melt pool length, L , across exposure time and scan speed. The upper limit of the temperature range is restricted by both the saturation and the flattening radiometric response curve. Saturation takes place when the number of photons entering the imaging sensor does not further increase the output signal. Fig. 9b shows the system's predicted sensible range of blackbody temperatures above the noise floor and below saturation for three different filter combinations across exposure time. The predicted signal was calculated by fitting Eq. (3) to the average red and green NIST blackbody signals. The maximum and minimum sensible temperature decreases with increasing exposure time. As noted in the introduction based on results from [1], for common AM metals with melting temperatures around 1700 K, the maximum spectral emissive power occurs at $1.7 \mu\text{m}$, and the peak shifts to $0.7 \mu\text{m}$ around temperatures of 4000 K. Therefore, for imaging applications that are light-limited, IR sensors are superior for measuring temperatures around the melting point of AM materials, and visible cameras are superior for measuring peak melt pool temperatures.

Because the melt pool is at temperatures in excess of the vaporization temperature, some liquid metal vaporizes and forms a plume above

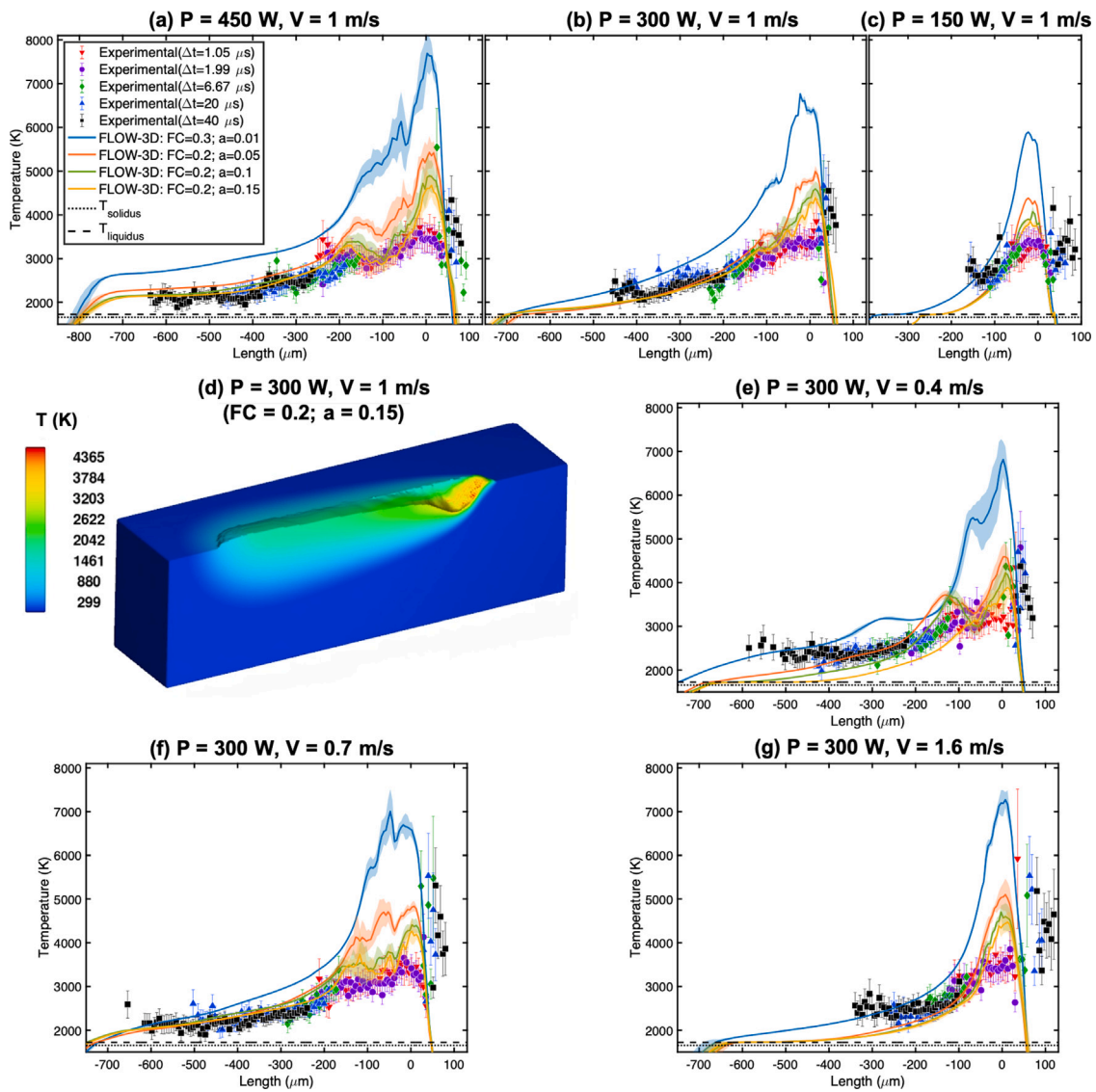


Fig. 8. Experimentally measured and FLOW-3D® predicted temperature profile near the 316L SS melt pool center-line along the melt pool length for a velocity of 1 m/s and power of (a) 450 W, (b) 300 W, and (c) 150 W. The four combinations of simulated accommodation and Fresnel coefficients shown had the best agreement to ex-situ geometry measurements (<20%). (d) Sliced FLOW-3D® simulation temperature field for a velocity of 1 m/s and power of 300 W with a Fresnel coefficient of 0.2 and accommodation coefficient of 0.15 (contoured at a fluid fraction of 0.5). Experimentally measured and FLOW-3D® predicted temperature profiles near the 316L SS melt pool center-line along the melt pool length for a velocity of power of 300 W and velocity of (e) 0.4 m/s, (f) 0.7 m/s, and (g) 1.6 m/s.

the melt pool. Overhead imaging of the melt pool can be obstructed by the plume [25], which is emitting, absorbing, and scattering light. Laser radiation is reflected off of the melt pool into the plume, causing bright, broadband incandescence of metal vapor, and possibility its ionization into plasma that would result in intense spectral peaks depending on the constituent elements rather than continuous blackbody emission [41]. This hot and optically dense part of the plume emission could be the cause of the high-temperature band surrounding the front of the melt pools in this work. Upon cooling, the metal vapor condenses and coalesces into larger particles. The filtering of light through a vapor plume from a laser welding process has been experimentally measured [42] and has been attributed to both absorption and scattering. This filtering of light by the plume would impact the temperature measurements by blocking the laser light reaching the melt pool surface, and spectrally filtering emission from the melt pool reaching the camera. Further investigation into the plume's emission and extinction will be necessary to fully understand how it affects the overhead melt pool temperature measurements and if it is possible to accurately measure the temperature within the plume itself. Optical

aberrations can also impact the measured ratios by blurring light at different wavelengths. Genzale et al. measured the focal positions for a lens train similar to the base lens system used in this work and found that the blue color's focal position was 1 mm further than the red and green colors' focal positions, which were nearly identical [43]. The blue color was not analyzed in this work.

5. Conclusion

We present surface temperature measurements of melt pools in laser powder bed fusion applying a single camera, multi-wavelength, high-speed imaging method. This method mitigates the need for complex alignment and could serve as a tool to understand the complex underlying physics, validate modeling methods, and improve in-situ process monitoring of melt pools in additive manufacturing. A key imaging parameter for this technique is exposure time, which impacts the sensible temperature range and motion blurring within the melt pool. Our thermal images for 316L SS show measured peak melt pool temperatures between 3300 K and 3700 K in the center of the melt pool,

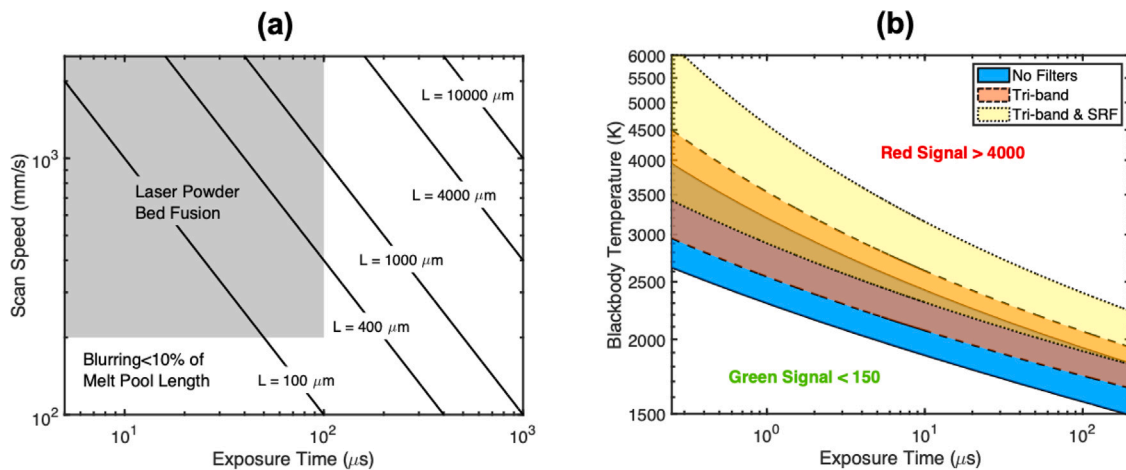


Fig. 9. (a) Contours across exposure time and scan speed where the blur within a frame is 10% of the melt pool length. (b) Predicted regions of blackbody temperature measurement bound by 150 and 4000 digital levels for three different filter combinations. As the exposure time is increased, the system becomes sensitive to lower temperatures as the green signal surpasses the noise floor.

and we compare them to thermal images of In718 and Ti-6Al-4V melt pools. Plume emission and transmission above the melt pool obscure the front and side melt pool boundaries in some images. Obstruction by the plume is material-dependent, with Ti-6Al-4V being the most severe. Although the plume obstructs imaging of the melt pool, it may also provide insight about how LPBF parameters influence its size and composition. CFD modeling shows that Fresnel coefficients ranging from 0.2 to 0.3 and accommodation coefficients ranging from 0.01 to 0.15 fit the melt track geometry but result in significantly different temperature profiles. Melt pool temperature measurements advance the state of validation and understanding of melt pool physics and could be used as an advanced process monitoring tool.

CRediT authorship contribution statement

Alexander J. Myers: Writing – review & editing, Writing – original draft, Visualization, Validation, Software, Methodology, Formal analysis, Investigation, Data curation, Conceptualization. **Guadalupe Quirarte:** Writing – review & editing, Writing – original draft, Visualization, Validation, Methodology, Formal analysis, Investigation, Data curation, Conceptualization. **Francis Ogoke:** Writing – review & editing, Software, Methodology. **Brandon M. Lane:** Writing – review & editing, Validation, Supervision, Methodology, Investigation. **Syed Zia Uddin:** Conceptualization. **Amir Barati Farimani:** Writing – review & editing, Supervision, Funding acquisition. **Jack L. Beuth:** Writing – review & editing, Supervision, Methodology, Funding acquisition. **Jonathan A. Malen:** Writing – review & editing, Visualization, Supervision, Resources, Methodology, Funding acquisition, Conceptualization.

Declaration of competing interest

The authors declare that they have no known competing financial interests or personal relationships that could have appeared to influence the work reported in this paper.

Data availability

Data will be made available on request

Acknowledgments

A portion of this research was sponsored by the Army Research Laboratory, USA and was accomplished under Cooperative Agreement Number W911NF-20-2-0175. The views and conclusions contained in this document are those of the authors and should not be interpreted as representing the official policies, either expressed or implied, of the Army Research Laboratory or the U.S. Government. The U.S. Government is authorized to reproduce and distribute reprints for Government purposes notwithstanding any copyright notation herein. This work is also supported by Army ERDC, USA Grant No. 1990749. G.Q. and A.J.M. and a portion of this research is supported by the National Science Foundation Graduate Research Fellowship Program, USA under Grant No. DGE2140739 & DGE1745016. Any opinions, findings, and conclusions or recommendations expressed in this material are those of the author(s) and do not necessarily reflect the views of the National Science Foundation. We thank Scott Kram, Christian Gobert, David Guirguis, and Todd Baer for their help with the LPBF machine and high-speed imaging equipment. Additionally, we thank Sergey Mekhontsev at NIST who assisted with the operation of the NIST high-temperature blackbody source. The authors acknowledge use of the Materials Characterization Facility at Carnegie Mellon University, USA supported by grant MCF-677785. We also acknowledge the use of the NextManufacturing facilities at Carnegie Mellon University.

Appendix A. Supplementary data

Supplementary material related to this article can be found online at <http://dx.doi.org/10.1016/j.addma.2023.103663>.

References

- [1] P.A. Hooper, Melt pool temperature and cooling rates in laser powder bed fusion, *Addit. Manuf.* 22 (2018) 548–559, <http://dx.doi.org/10.1016/j.addma.2018.05.032>.
- [2] S.K. Everton, M. Hirsch, P.I. Stavroulakis, R.K. Leach, A.T. Clare, Review of in-situ process monitoring and in-situ metrology for metal additive manufacturing, *Mater. Des.* 95 (2016) 431–445, <http://dx.doi.org/10.1016/j.matdes.2016.01.099>.
- [3] B. Cheng, L. Loeber, H. Willeck, U. Hartel, C. Tuffile, Computational investigation of melt pool process dynamics and pore formation in laser powder bed fusion, *J. Mater. Eng. Perform.* 28 (11) (2019) 6565–6578, <http://dx.doi.org/10.1007/s11665-019-04435-y>.

- [4] L. Caprio, A.G. Demir, B. Previtali, Observing molten pool surface oscillations during keyhole processing in laser powder bed fusion as a novel method to estimate the penetration depth, *Addit. Manuf.* 36 (2020) <http://dx.doi.org/10.1016/j.addma.2020.101470>.
- [5] K. Taherkhani, E. Sheydaei, C. Eisler, M. Otto, E. Toyserkani, Development of a defect-detection platform using photodiode signals collected from the melt pool of laser powder-bed fusion, *Addit. Manuf.* 46 (2021) <http://dx.doi.org/10.1016/j.addma.2021.102152>.
- [6] C.G. Ren, Y.L. Lo, H.C. Tran, M.H. Lee, Emissivity calibration method for pyrometer measurement of melting pool temperature in selective laser melting of stainless steel 316L, *Int. J. Adv. Manuf. Technol.* 105 (2019) 637–649, <http://dx.doi.org/10.1007/s00170-019-04193-0>.
- [7] J.M. Densmore, M.M. Biss, K.L. McNesby, B.E. Homan, High-speed digital color imaging pyrometry, *Appl. Opt.* 50 (17) (2011) 2659–2665.
- [8] K. McNesby, S. Dean, R. Benjamin, J. Grant, J. Anderson, J. Densmore, Imaging pyrometry for most color cameras using a triple pass filter, *Rev. Sci. Instrum.* 92 (2021) <http://dx.doi.org/10.1063/5.0037230>.
- [9] C.K.P. Vallabh, X. Zhao, Melt pool temperature measurement and monitoring during laser powder bed fusion based additive manufacturing via single-camera two-wavelength imaging pyrometry (STWIP), *J. Manuf. Process.* 79 (2022) 486–500, <http://dx.doi.org/10.1016/j.jmapro.2022.04.058>.
- [10] J.A. Mitchell, T.A. Ivanoff, D. Dage, J.D. Madison, B. Jared, Linking pyrometry to porosity in additively manufactured metals, *Addit. Manuf.* 31 (2020) <http://dx.doi.org/10.1016/j.addma.2019.100946>.
- [11] S. Barua, F. Liou, J. Newkirk, T. Sparks, Vision-based defect detection in laser metal deposition process, *Rapid Prototyp. J.* 20 (1) (2014) 77–86, <http://dx.doi.org/10.1108/RPJ-04-2012-0036>.
- [12] T. Kuriya, R. Koike, T. Mori, Y. Kakinuma, Relationship between solidification time and porosity with directed energy deposition of Inconel 718, *J. Adv. Mech. Des. Syst. Manuf.* 12 (5) (2018) <http://dx.doi.org/10.1299/jamdsm.2018jamdsm0104>.
- [13] Photron, FASTCAM mini AX hardware manual, 2021, URL <https://photron.com/>.
- [14] B.E. Bayer, *Color Imaging Array*, Eastman Kodak Co, 1976.
- [15] D.X. Qu, J. Berry, N.P. Calta, M.F. Crumb, G. Guss, M.J. Matthews, Temperature measurement of laser-irradiated metals using hyperspectral imaging, *Phys. Rev. A* 14 (1) (2020) <http://dx.doi.org/10.1103/PhysRevApplied.14.014031>.
- [16] Y.S. Touloukian, D.P. DeWitt, *Thermal Radiative Properties Metallic Elements and Alloys*, Vol. 7, CINDAS/Purdue University, Lafayette, IN, 1970.
- [17] H. Malvar, L. wei He, R. Cutler, High-quality linear interpolation for demosaicing of Bayer-patterned color images, in: 2004 IEEE International Conference on Acoustics, Speech, and Signal Processing, Vol. 3, 2004, pp. iii–485, <http://dx.doi.org/10.1109/ICASSP.2004.1326587>.
- [18] S.E.P., P. Kreth, Photron MRAW File Reader, MATLAB Central File Exchange, 2021, <https://www.mathworks.com/matlabcentral/answers/814495-how-to-read-a-mraw-file>. <https://www.mathworks.com/matlabcentral/fileexchange/42408-photron-mraw-file-reader>.
- [19] P.E. Debevec, J. Malik, Recovering high dynamic range radiance maps from photographs, in: *ACM SIGGRAPH 2008 Classes*, 2008, pp. 1–10.
- [20] B.A. Fisher, Part Temperature Effects in Powder Bed Fusion Additive Manufacturing of Ti-6Al-4V (Ph.D. thesis), Carnegie Mellon University, Pittsburgh, 2018, <http://dx.doi.org/10.1184/R1/6720995.v1>.
- [21] D.C. Deisenroth, S. Mekhontsev, B. Lane, L. Hanssen, I. Zhironov, V. Khromchenko, S. Grantham, D. Cardenas-Garcia, A. Donmez, Measurement uncertainty of surface temperature distributions for laser powder bed fusion processes, *J. Res. Natl. Inst. Stand. Technol.* 126 (2021) 1–65, <http://dx.doi.org/10.6028/JRES.126.013>.
- [22] K. Hoshino, H. Sumi, T. Nishimura, Noise detection and reduction for image sensor by time domain autocorrelation function method, in: *IEEE International Symposium on Industrial Electronics*, 2007, pp. 1737–1740.
- [23] S. Farsiu, M. Elad, P. Milanfar, Multiframe demosaicing and super-resolution of color images, *IEEE Trans. Image Process.* 15 (2006) 141–159, <http://dx.doi.org/10.1109/TIP.2005.860336>.
- [24] K.C. Mills, Fe-316 stainless steel, in: *Recommended Values of Thermophysical Properties for Selected Commercial Alloys*, Woodhead Publishing, 2002, pp. 135–142, URL <https://app.knovel.com>.
- [25] C.B. Stutzman, W.F. Mitchell, A.R. Nassar, Optical emission sensing for laser-based additive manufacturing—What are we actually measuring? *J. Laser Appl.* 33 (1) (2021) 012010, <http://dx.doi.org/10.2351/7.0000321>.
- [26] J.P. Oliveira, A.D. LaLonde, J. Ma, Processing parameters in laser powder bed fusion metal additive manufacturing, *Mater. Des.* 193 (2020) <http://dx.doi.org/10.1016/j.matdes.2020.108762>.
- [27] C. Barrett, C. Carradero, E. Harris, K. Rogers, E. MacDonald, B. Conner, Statistical analysis of spatter velocity with high-speed stereovision in laser powder bed fusion, *Progr. Addit. Manuf.* 4 (2019) 423–430, <http://dx.doi.org/10.1007/s40964-019-00094-6>.
- [28] D. Rosenthal, Mathematical theory of heat distribution during welding and cutting, *Weld. J.* 20 (1941) 220–234.
- [29] T.W. Eagar, N.S. Tsai, Temperature Fields Produced by Traveling Distributed Heat Sources Use of a Gaussian heat distribution in dimensionless form indicates final weld pool shape can be predicted accurately for many welds and materials, *Weld. J.* 62 (12) (1983) 346–355.
- [30] A.V. Gusarov, I. Yadroitsev, P. Bertrand, I. Smurov, Model of radiation and heat transfer in laser-powder interaction zone at selective laser melting, *J. Heat Transfer* 131 (2009) 1–10, <http://dx.doi.org/10.1115/1.3109245>.
- [31] H.C. Tran, Y.L. Lo, Heat transfer simulations of selective laser melting process based on volumetric heat source with powder size consideration, *J. Mater. Process. Technol.* 255 (2018) 411–425, <http://dx.doi.org/10.1016/j.jmatprotec.2017.12.024>.
- [32] Flow Science, FLOW-3D, Version 11.2, Santa Fe, NM, 2019, URL <https://www.flow3d.com/>.
- [33] C.W. Hirt, B.D. Nichols, Volume of fluid (VOF) method for the dynamics of free boundaries, *J. Comput. Phys.* 39 (1) (1981) 201–225.
- [34] A. Hemmasian, F. Ogoke, P. Akbari, J. Malen, J. Beuth, A.B. Farimani, Surrogate modeling of melt pool thermal field using deep learning, 2022, arXiv preprint [arXiv:2207.12259](https://arxiv.org/abs/2207.12259).
- [35] J.L. Tan, C. Tang, C.H. Wong, A computational study on porosity evolution in parts produced by selective laser melting, *Metallurg. Mater. Trans. A Phys. Metall. Mater. Sci.* 49 (8) (2018) 3663–3673, <http://dx.doi.org/10.1007/s11661-018-4697-x>.
- [36] J. Trapp, A.M. Rubenchik, G. Guss, M.J. Matthews, In situ absorptivity measurements of metallic powders during laser powder-bed fusion additive manufacturing, *Appl. Mater. Today* 9 (2017) 341–349.
- [37] W. Schulz, G. Simon, H. Urbassek, I. Decker, On laser fusion cutting of metals, *J. Phys. D: Appl. Phys.* 20 (4) (1987) 481.
- [38] R. Ducharme, K. Williams, P. Kapadia, J. Dowden, B. Steen, M. Glowacki, The laser welding of thin metal sheets: an integrated keyhole and weld pool model with supporting experiments, *J. Phys. D: Appl. Phys.* 27 (8) (1994) 1619.
- [39] I. Bitharas, N. Parab, C. Zhao, T. Sun, A.D. Rollett, A.J. Moore, The interplay between vapour, liquid, and solid phases in laser powder bed fusion, *Nature Commun.* 13 (2022) <http://dx.doi.org/10.1038/s41467-022-30667-z>.
- [40] S.A. Khairallah, A.T. Anderson, A. Rubenchik, W.E. King, Laser powder-bed fusion additive manufacturing: Physics of complex melt flow and formation mechanisms of pores, spatter, and denudation zones, *Acta Mater.* 108 (2016) 36–45, <http://dx.doi.org/10.1016/j.actamat.2016.02.014>.
- [41] I. Miyamoto, T. Uchida, H. Maruo, T. Arai, Mechanism of soot deposition in laser welding, in: *International Congress on Applications of Lasers and Electro-Optics*, Vol. 1994, No. 1, 1994, pp. 293–302, <http://dx.doi.org/10.2351/1.5058801>.
- [42] P.Y. Shcheglov, A.V. Gumenyuk, I.B. Gornushkin, M. Rethmeier, V.N. Petrovskiy, Vapor-plasma plume investigation during high-power fiber laser welding, *Laser Phys.* 23 (1) (2013) <http://dx.doi.org/10.1088/1054-660X/23/1/016001>.
- [43] C. Genzale, Spatially and Temporally Resolved Imaging of Primary Breakup in High-Pressure Fuel Sprays, Georgia Tech Research Corporation, Atlanta, 2019.